ACS Catalysis

pubs.acs.org/acscatalysis Research Article

Hydrogen Bonding-Mediated Enhancement of Bioinspired Electrochemical Nitrogen Reduction on $Cu_{2-x}S$ Catalysts

Min-Cheol Kim,[#] Hyunji Nam,[#] Jihyun Choi,[#] Hee Soo Kim, Hong Woo Lee, Donghun Kim, Jimin Kong, Sang Soo Han,* Seung Yong Lee,* and Hyun S. Park*

Cite This: *ACS Catal.* 2020, 10, 10577−10584 Read Online

ACCESS | Metrics & More | Article Recommendations | Supporting Information

ABSTRACT: The electrochemical nitrogen reduction reaction (NRR) has been regarded as a promising alternative to the conventional Haber−Bosh process for NH_3 synthesis. Inspired by the Fe−Mo−S cofactor in the enzyme nitrogenase, metal sulfide catalysts, mostly Fe- or Mo-based sulfides, have recently received great interest. Here, we propose $Cu_{2-x}S$ ($0 \le x < 1$) as an efficient NRR electrocatalyst. Electrochemical tests at room temperature and atmospheric pressure reveal that $Cu_{1.81}S$ achieves a high NH_3 yield of 2.19 μmol h^{-1} cm^{-2} along with a Faradaic efficiency of 14.1% at −0.1 V versus reversible hydrogen electrode in an aqueous electrolyte. According to our first-principles calculations, the superior NRR properties originate from the threefold-coordinate Cu sites in $Cu_{1.81}S$. These sites enable N−H···S hydrogen bonding during N_2H_y adsorption and stabilize the intermediates on the $Cu_{2-x}S$ surfaces, leading to a significant decrease in the overpotential limit for the NRR. Moreover, the threefold sites not only provide a bioinspired NRR pathway similar to that of nitrogenase but also enable both distal and alternating pathways, increasing the efficiency for the NRR. This study presents an attractive electrocatalyst for the NRR and opens an alternative route to explore chalcogenides and halides as NRR catalysts where the hydrogen-bonding mediation can similarly operate.

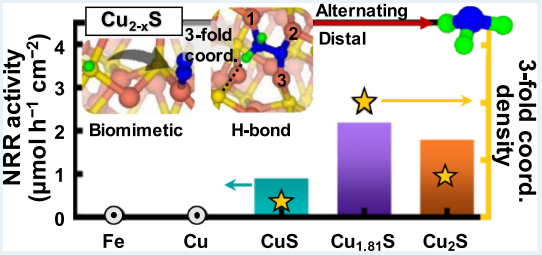

KEYWORDS: *nitrogen reduction reaction, electrocatalysis, bioinspired, nitrogenase, mechanism, copper sulfide, density functional theory*

1. INTRODUCTION

Ammonia (NH_3) production from nitrogen reduction is an important chemical reaction academically and industrially. Currently, the Haber−Bosch process enables mass production of ammonia, which is critical in supporting half of the world population via its role of an essential precursor in fertilizer production.[1] However, the process can be operated only under high temperatures (400−500 °C) and pressures (10−30 MPa) because of the notoriously strong N_2 triple bond.[2] Recently, an electrochemical nitrogen reduction reaction (NRR) under ambient conditions has been of great interest as an alternative,[3−6] although it is still extremely challenging to realize an NRR catalyst with a high ammonia production rate and selectivity.[7]

Inspired by the enzyme nitrogenase and its Fe−Mo−S cofactor in the active site,[8,9] the NRR activities of metal sulfide catalysts such as FeS_2,[10,11] MoS_2,[12] and FeS−MoS_2 composites[13] have been recently explored. Although these materials have shown promise for the NRR, there is still room to enhance the NRR activity by further reproducing the NRR mechanism of nitrogenase as follows: (1) formation of more metal−nitrogen(−metal) bonds that are crucial to bind N_xH_y intermediates during the NRR and (2) generation of sulfur sites to facilitate proton transfer (PT) to N_2.[9] For these steps, it is necessary to further increase the number of active metal-binding sites on the metal sulfide surfaces.

Fe and Mo prefer an oxidation number of 2 or higher; thus, it is difficult to design sulfide catalysts with metal/sulfur ratios higher than 1. However, Cu can exhibit an oxidation number as low as 1, hence leading to a variety of $Cu_{2-x}S$ ($0 \le x < 1$) structures. According to previous reports on copper sulfides,[14,15] mostly for the CuS (Cu/S = 1:1) system, they showed low NRR activity. In this work, we focus on $Cu_{2-x}S$ ($0 \le x < 1$) catalysts for the NRR and find that they show an NH_3 yield rate as high as 2.19 μmol h^{-1} cm^{-2} and a Faradaic efficiency (FE) of 14.1%. Our first-principles density functional theory (DFT) calculations reveal that the enhancement in the NRR indeed originates from the $Cu_{2-x}S$ catalysts proceeding through a bioinspired NRR pathway similar to that of nitrogenase.

2. THEORETICAL AND EXPERIMENTAL DETAILS

2.1. Preparation of $Cu_{2-x}S$ Catalysts. $Cu_{2-x}S$ samples were synthesized by a combination of the dry mechanochemical method and wet milling method. CuS and Cu_2S particles

Received: April 17, 2020
Revised: August 20, 2020
Published: August 24, 2020

https://dx.doi.org/10.1021/acscatal.0c01730
ACS Catal. 2020, 10, 10577−10584

were first synthesized by the dry mechanochemical method. In the mechanochemical method, a steel jar containing precursors and balls was rotated at 550 rpm with spinning for up to 2 h in a planetary ball mill machine (Fritsch GmBH, Pulverisette 5 classic line). Elemental Cu (Alfa Aesar, 99.9%, ~100 mesh) and S (Sigma-Aldrich, 99.8%) powders were used as precursors. The elemental precursors were weighed under an argon atmosphere in a glovebox with the determined ratios (Cu/S = 1:1 and 2:1). The powder mixture (5 g) and ZrO_2 balls (25 g of 5 mm ⌀ balls and 25 g of 10 mm ⌀ balls) were charged into a stainless steel jar (approximately 80 mL in volume) without any solvents or any additives. The ratio of the ball to the precursor was fixed at 10:1 in weight percent. After ball milling, the as-synthesized particles were post-annealed at 400 °C for 2 h in a tube furnace under an Ar (99.999%) gas atmosphere.

After the preparation of the CuS and Cu_2S samples, they underwent the wet-milling process in order to generate inks for coating the NRR electrode. The samples (2 g), 8 mL of isopropyl alcohol, and 45 g of ZrO_2 balls (1 mm ⌀/5 mm ⌀ = 2:1) were loaded in a Nalgene bottle. The bottle was rotated at 200 rpm. CuS catalysts were obtained after 72 h milling of the CuS samples. $Cu_{1.81}S$ catalysts were obtained after 72 h milling of the Cu_2S samples, and Cu_2S catalysts were obtained after 12 h milling of the Cu_2S samples.

2.2. Synthesis of Cu Catalysts. First, 500.0 mg (2.15 mmol) of copper nitrate hemipentahydrate [$Cu(NO_3)_2 \cdot 2.5H_2O$, Sigma-Aldrich, 99.9%] was dissolved in 15 mL of dimethylformamide (DMF, Sigma-Aldrich, 99.9%), and then, 301.2 mg (1.43 mmol) of trimesic acid (H_3btc, Sigma-Aldrich, 99.9%) was added. After stirring for 30 min, the solution was kept in a glass vial at 80 °C for 6 h and then cooled to room temperature. Blue crystals (Cu-HKUST-1) were obtained. After washing with DMF and solvent-exchanged with acetonitrile (MeCN, Sigma-Aldrich, 99.9%) for 1 d, the product was heated to 80 °C under a static vacuum for 12 h. The as-synthesized Cu-HKUST-1 was added to a crucible, which was then placed in a tube furnace and heated to 800 °C under Ar (99.999%) with a heating rate of 4.3 °C/min. After reaching the target temperature, the material was maintained for 3 h and then naturally allowed to cool to room temperature.

2.3. Synthesis of Fe Catalysts. First, 0.04 M iron(II)-chloride (0.238 g, $FeCl_2 \cdot 4H_2O$, Sigma-Aldrich, 99.9%) was dissolved in 30 mL of ethanol under mechanical stirring to obtain a clear homogeneous solution. Next, 0.1 M sodium borohydride (0.378 g, $NaBH_4$, Sigma-Aldrich, 99.9%) dissolved in 100 mL of DI water was added dropwise to the abovementioned solution. During the addition process, the color of the solution changed from orange to dark red, which in turn resulted in a black precipitate. The precipitates were collected by centrifugation, washed several times using ethanol and DI water, and finally dried at 70 °C under a vacuum. To obtain a pure Fe crystal phase of the catalyst, the as-synthesized Fe samples were added to a crucible, which was then placed in a tube furnace and heated to 600 °C under H_2 (99.9%) with a heating rate of 10 °C/min. After reaching the target temperature, the catalyst was maintained for 6 h and then naturally allowed to cool to room temperature.

2.4. Material Characterization. Transmission electron microscopy (TEM) images and energy-dispersive X-ray spectroscopy (EDS) spectra were acquired using a scanning transmission electron microscope (FEI Talos F200X) equipped with an energy-dispersive spectrometer (EDS) (Bruker Super-X EDS system). The crystal structure and phase purity were examined by X-ray diffraction (XRD) with Cu Kα radiation (λ = 1.5406 Å).

2.5. Electrochemical Experiments. A Bio-Logic SP-300 potentiostat was used for all electrochemical experiments. The electrochemical experiments were performed at room temperature and pressure. For the three-electrode configuration, the metal sulfide working electrodes were studied by employing a standard calomel electrode and graphite rod as the reference electrode and counter electrode, respectively. All potentials were converted to the reversible hydrogen electrode (RHE) scale. Wet-milled $Cu_{2-x}S$ catalysts were hand-sprayed onto a carbon paper (2.5 cm × 2.5 cm, Toray T-120) and dried in a desiccator at ambient temperature. The amount of catalyst to be coated onto the electrode was 1 mg cm^{-2}. The coated electrode was rinsed with 0.1 M KOH (pH 13.3) before starting the experiment. The electrolyte used was 0.1 M KOH (85%, Sigma), and the absorber (Trap solution) was 10 mM H_2SO_4. Anion-exchange membranes (FAA-3, Fumatech) were used to separate the cathode and anode chambers and were immersed in 1 M KOH for 24 h and DI water for another 1 h before the NRR tests. Chronoamperometry (CA) was performed for 1 h each at different potentials to accumulate the NH_3 produced in the electrolyte solution under controlled atmosphere at room temperature. For the electrochemical NRR, $^{14}N_2$ (99.999%) and $^{15}N_2$ (98 atom %, Sigma) were bubbled for approximately 20 min before the measurements and continuously purged into the cathode compartment during the experiments, with the flow rates of 250 and 5 cm^3/min, respectively.

2.6. Quantification of Ammonia. The concentration of produced ammonia was determined by the indophenol blue method. For this method, 1 mL of aliquot taken from the cathode electrolyte solution or trap solution was mixed with 1 mL of a phenol solution (0.64 M C_6H_5OH, 0.38 M NaOH, and 1.3 mM $C_5FeN_6Na_2O$) and 1 mL of hypochlorite solution (55 mM NaOCl and 0.75 M NaOH). After 1 h of reaction at room temperature, the sample absorbance was analyzed by UV−vis spectroscopy (Cary UV−visible 100 spectrophotometer, Agilent) from 900 to 350 nm. The indophenol absorbance peaks were measured at 633 nm after subtracting the background absorbance measured at 875 nm. The concentration−absorbance curves were calibrated with the Beer−Lambert law

$$A = \varepsilon bc \tag{1}$$

where A is the absorbance, ε is the extinction coefficient, b is the UV−vis quartz cuvette length of 1 cm, and c is the sample concentration. The standard ammonium chloride solutions within the range of 0−10 ppm (0, 0.25, 0.50, 0.75, 2.50, 5.00, 7.50, and 10.00 ppm) are used for calibration. The estimated extinction coefficient is 267 ± 57 L mol^{-1} cm^{-1}.

2.7. NMR Spectroscopy. Both $^{14}N_2$ and $^{15}N_2$ were analyzed by ^{1}H NMR (nuclear magnetic resonance, Bruker ADVANCE III HD 400 MHz) spectroscopy to identify the electrochemically produced ammonia. After electrolysis, the pH of the electrolyte aliquot was adjusted to 2 by adding 1 M H_2SO_4. Then, 10 vol % D_2O (99.994 atom % D, Sigma-Aldrich) was added to the analyte solution for NMR measurements. The samples in all NMR experiments were scanned for 400 cycles.

https://dx.doi.org/10.1021/acscatal.0c01730
ACS Catal. 2020, 10, 10577−10584

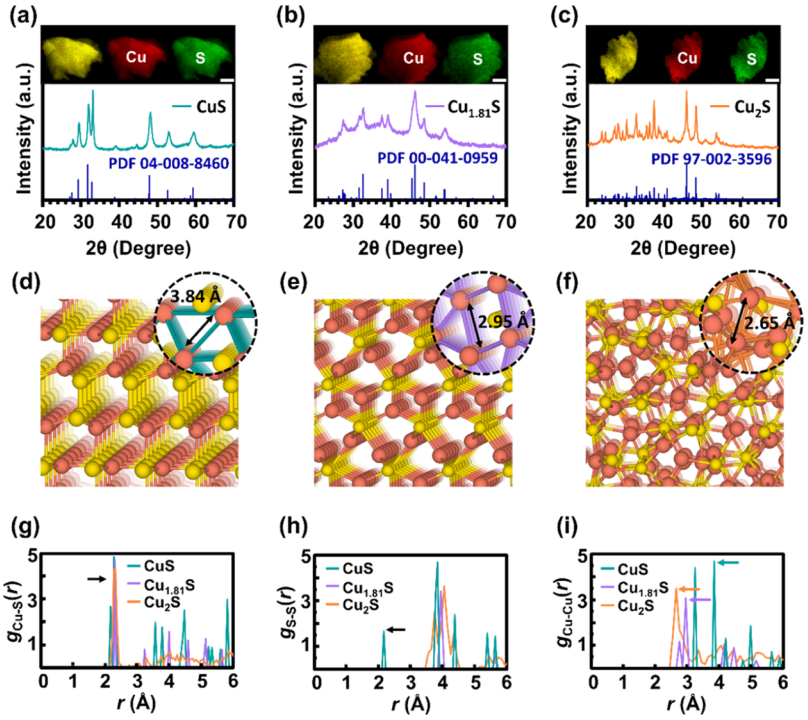

Figure 1. (a–c) Experimental TEM images with EDS mapping and XRD patterns of the synthesized CuS (a), $Cu_{1.81}S$ (b), and Cu_2S (c), where the scale bar in the TEM images is 70 nm. (d–f) Atomic structures for CuS (d), $Cu_{1.81}S$ (e), and Cu_2S (f). Here, the color code for atoms is coral = Cu and yellow = S. (g–i) RDFs for the Cu–S (g), S–S (h), and Cu–Cu (i) pairs in the copper sulfides. The insets in (d–f) depict the Cu–Cu distances from the major Cu–Cu RDF peaks represented by the arrows in (i).

2.8. Determination of Ammonia Yield and FE. The FE of N_2 reduction was calculated as follows

$$\text{F. E. } (\%) = 100 \times \frac{n \times F \times [NH_3]}{Q} \tag{2}$$

The NH_3 formation rate r_{NH_3} is estimated by

$$r_{NH_3}\ (\text{mol h}^{-1}\ \text{cm}^{-2}) = \frac{[NH_3]}{t \times A} \tag{3}$$

where n is the number of electrons, F is the Faraday constant (96,485 [C/mol]), $[NH_3]$ is the total amount of NH_3 detected at different potentials in the electrolyte and trap solution, Q is the total charge (current × time), t is the reaction time, and A is the surface area.

2.9. First-Principles Calculations. All of the first-principles DFT calculations were performed using the Vienna Ab initio Simulation Package[16] with the revised Perdew–Burke–Ernzerhof[17] functional as the exchange and correlation functional with the D3 dispersion correction.[18] The projector-augmented-wave method was adopted to describe the potential from the ionic core,[19] and an energy cutoff of 500 eV was used. Monkhorst–Pack k-point sampling with the k-point spacing <0.03 $Å^{-1}$ was used for all systems. The spin polarization and dipole correction were also included. For nonelectrochemical reactions, the climbing-image nudged elastic band[20] method was employed to calculate the transition state for the reaction step.

Because a unit cell of tetragonal $Cu_{1.81}S$ includes 73 atoms (Cu: 47, S: 26), a first-principles investigation of its NRR process is very challenging, which requires a simple slab model for the system. Fortunately, the space group of tetragonal $Cu_{1.81}S$ ($P4_32_12$, no. 96) is the same as that of tetragonal Cu_2S (unit cell: 8 Cu, 4 S),[21] implying that the majority of local atomic structures in $Cu_{1.81}S$ are similar to those in Cu_2S; thus, tetragonal Cu_2S can be readily regarded as a model of $Cu_{1.81}S$ for NRR calculation. Then, the flat surfaces of $Cu_{1.81}S$ were modeled with four-layer slabs repeated periodically. The top two layers of the slab models and the adsorbates were allowed to relax until the forces on the individual relaxed atoms were less than 0.03 eV $Å^{-1}$, whereas the bottom two layers were fixed during the optimization process.

For the tetragonal $Cu_{1.81}S$ slab model, all of the possible cleavages were scanned for several low-index surfaces such as (001), (100), (101), (110), and (111) to find the most stable structure for the NRR pathway calculation (Figure S1); the number of atoms for each slab model was 12, 24, 24, 48, and 48, respectively. Here, a vacuum spacing of >15 Å was used to prevent interslab interactions in the slab systems. Our first-principles calculations reveal that the (111) surface has the lowest energy (Figure S1), and we explore the NRR mechanisms over $Cu_{1.81}S(111)$ at U = 0 V and pH 13.3.

To investigate the full NRR pathways over the $Cu_{1.81}S$ surfaces, we considered all of the elementary steps for the NRR. The distal mechanism can be depicted as follows

$$N_2 + H^+ + e^- \rightarrow *NNH \tag{4}$$

$$*NNH + H^+ + e^- \rightarrow *NNH_2 \tag{5}$$

$$*NNH_2 + H^+ + e^- \rightarrow *N + NH_3 \tag{6}$$

$$*N + H^+ + e^- \rightarrow *NH \tag{7}$$

$$*NH + H^+ + e^- \rightarrow *NH_2 \tag{8}$$

$$*NH_2 + H^+ + e^- \rightarrow *NH_3 \tag{9}$$

https://dx.doi.org/10.1021/acscatal.0c01730
ACS Catal. 2020, 10, 10577–10584

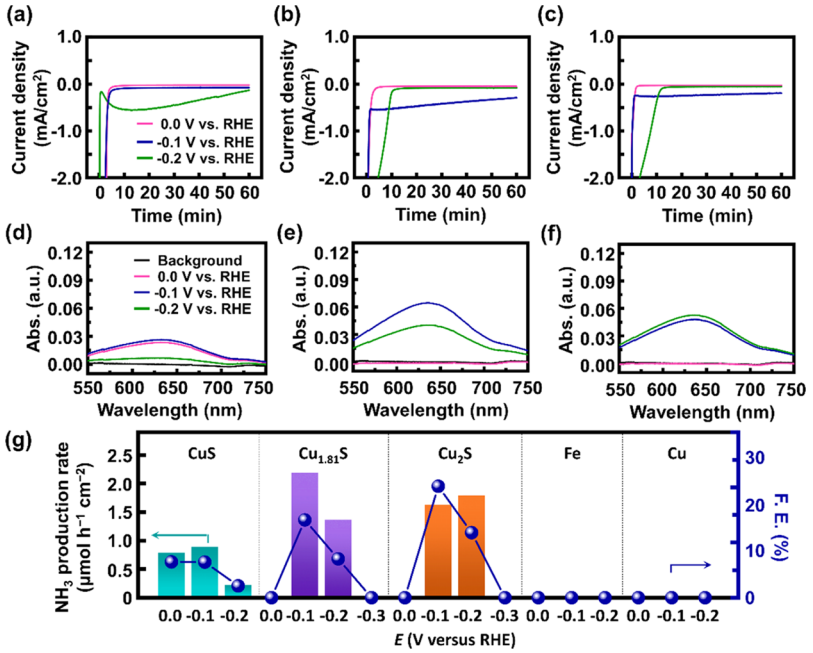

Figure 2. Electrochemical experiment results. (a–c) CA results and (d–f) UV–vis spectroscopy results of the electrolyte for CuS, $Cu_{1.81}S$, and Cu_2S. (g) Ammonia production yield and FE for the CuS, $Cu_{1.81}S$, and Cu_2S samples. For comparison, the results of monometallic Fe and Cu tested in this work are included.

$$*NH_3 \rightarrow NH_3 + * \quad (10)$$

Then, the bioinspired mechanism for $Cu_{2-x}S$ branching from eq 4 into eq 5 is

$$N_2 + (Cu)* \rightarrow (Cu)*N_2 \quad (11)$$

$$(S)* + H^+ + e^- \rightarrow (S)*H \quad (12)$$

$$(Cu)*N_2 + (S)*H \rightarrow *NNH \quad (13)$$

The mixed mechanism branching from eq 5 into eq 8 is

$$*NNH + H^+ + e^- \rightarrow *NHNH \quad (14)$$

$$*NHNH + H^+ + e^- \rightarrow *NHNH_2 \quad (15)$$

$$*NHNH_2 + H^+ + e^- \rightarrow *NH + NH_3 \quad (16)$$

The alternative mechanism branching from eq 15 into eq 9 is

$$*NHNH_2 + H^+ + e^- \rightarrow *NH_2NH_2 \quad (17)$$

$$*NH_2NH_2 + H^+ + e^- \rightarrow *NH_2 + NH_3 \quad (18)$$

To calculate the Gibbs free energy change of each elementary step involving PT and electron transfer, the potential under standard reaction conditions (298 K and 1 atm) was set as the reference potential, in which the chemical potential of the $(H^+ + e^-)$ pair was related to half of the chemical potential of a hydrogen gas molecule (H_2) at pH 0.[22] To directly compare our calculations with experiments, we considered pH 13.3 in the NRR pathways as in our experiments. For each step, $\Delta G = \Delta H + T\Delta S + \Delta E_{ZPE} + \Delta G_U + \Delta G_{pH}$. Here, the enthalpy $H = E + E_{ZPE} + \int_0^T C_V\, dT$, where E is the electronic energy, E_{ZPE} is the zero-point correction energy, and the last term is the integration of heat capacity. T is the absolute temperature and S is the entropy. E_{ZPE}, $\int_0^T C_V\, dT$, and S can all be derived from the vibrational frequencies of the adsorbed species, which are evaluated from finite-difference calculations. E, E_{ZPE}, $\int_0^T C_V\, dT$, and TS of the reference gas molecules (N_2, H_2, and NH_3) are presented in Table S1. ΔG_U represents the effect of the applied bias and is equal to $-neU$, in which n is the number of transferred electrons in each step. ΔG_{pH} is the contribution of H^+ and is equal to $-k_B \times \ln(10) \times pH$, where k_B is the Boltzmann constant. Solvation effects were not included because the solvation-induced stabilization of adsorbates in the NRR on metal surfaces is within 0.1–0.2 eV.[23]

3. RESULTS AND DISCUSSION

3.1. Catalyst Synthesis and Characterization. Two types of $Cu_{2-x}S$ catalysts, tetragonal $Cu_{1.81}S$ (space group: $P4_32_12$, no. 96) and chalcocite Cu_2S ($P2_1/c$, 14), in addition to the covellite CuS ($P6_3/mmc$, 194) catalyst, were prepared by a simple wet-milling method, and their crystal structures were confirmed by the XRD patterns (Figure 1a–c and Table S2). Additionally, the TEM and EDS results show that Cu and S are well dispersed in the particles (insets in Figure 1a–c). To further investigate the atomic structures of the catalysts, radial distribution functions (RDFs) for Cu–Cu, S–S, and Cu–S pairs were calculated (Figure 1g–i). In all three copper sulfides, Cu is bonded only to S with no Cu–Cu bond (Figure S2), where the Cu–S distances are all similar (2.3 Å). However, unlike $Cu_{1.81}S$ and Cu_2S, CuS includes S–S covalent bonds, and the major RDF peak for the Cu–Cu pair in CuS is much larger (3.8 Å) than those (2.7–3.0 Å) in $Cu_{1.81}S$ and Cu_2S, showing that the Cu sites in $Cu_{2-x}S$ are more closely packed over CuS. From these results, the $Cu_{2-x}S$ catalyst is expected to show a NRR activity superior to that of CuS. On the other hand, the particle sizes of the synthesized samples are in the range of 1.6–2.6 μm (Figure S3), and their Brunauer–Emmett–Teller surface areas are evaluated to be as low as < 10 m^2/g, which indicates that their nanosize effect on the NRR activity is not significant.

https://dx.doi.org/10.1021/acscatal.0c01730
ACS Catal. 2020, 10, 10577–10584

3.2. Electrochemical Reduction of N_2 to NH_3. Electrochemical measurements were carried out on a two-compartment cell (H cell) with a trap at room temperature and atmospheric pressure. Nitrogen (^{14}N and ^{15}N) was fed into the cathodic electrolyte by gas bubbling during the electrolysis. CA was used to measure the current density during the electrolysis (Figure 2a–c). The produced ammonia was measured with colorimetric assays using the indophenol blue method and NMR spectra (Figures 2d–f, S4, and S5). Additional tests were carried out to exclude possible interference from any contaminants (Figure S6), which included the following: (1) argon-saturated solution with the catalyst electrolyzed for 1 h, (2) electrolytes saturated by N_2 with a bare carbon paper, or (3) electrolytes saturated by N_2 with an open circuit for 1 h. No ammonia could be detected in the control experiments and in the traps (Figure S7). In addition, $^{15}NH_4^+$ was detected by NMR when $^{15}N_2$ was used as the dinitrogen source (Figure S5b). We also compare the electrochemical results with monometallic Cu and Fe nanoparticles (Figures S8 and S9). In Figure 2g, although monometallic Cu and Fe show no NRR performance, the optimal NRR activity over CuS is detected at −0.10 V (vs RHE) with a production rate of 0.89 μmol h^{-1} cm^{-2} and FE of 6.5%, and Cu_2S shows a production rate of 1.79 μmol h^{-1} cm^{-2} and FE of 11.8% at −0.20 V, indicating that the higher Cu content leads to a higher NRR activity, as initially intended. On the other hand, it is remarkable that the highest NRR activity is observed over the $Cu_{1.81}S$ catalyst, with a production rate of 2.19 μmol h^{-1} cm^{-2} and FE of 14.1% at −0.10 V. This production rate was also confirmed with the ^1H NMR analysis, revealing the production rate of 2.29 μmol h^{-1} cm^{-2} (Figure S5). Note that $Cu_{1.81}S$ shows a higher NH_3 production rate and FE than those of the most reported metal sulfide catalysts under ambient conditions, including MoS_2 (0.29 μmol h^{-1} cm^{-2}, 1.2%;[24] 0.15 μmol h^{-1} cm^{-2}, 4.6%[12]) and FeS_2 (0.14–0.28 μmol h^{-1} cm^{-2}[11]). A comparison with other reported electrocatalysts is summarized in Table S3.

3.3. First-Principles NRR Mechanism Study on $Cu_{1.81}S$ Surface. To gain insight into the NRR activity of copper sulfides, we performed a mechanistic study of the NRR on the $Cu_{1.81}S$ surface using a DFT method. It was reported that electrochemical N_2 reduction preferentially operates via an associative mechanism rather than a dissociative mechanism.[23,25] Based on the associative process, we carefully investigated the NRR mechanism over $Cu_{1.81}S$ by DFT calculations and then compared it with those over Cu and Fe surfaces (Figure 3). Here, the distal, alternating, and mixed pathways[26,27] for the associative NRR were considered. The mixed route is similar to the alternating route up to the third protonation, leading to the formation of $*N_2H_3$; however, a further protonation of $*N_2H_3$ leads to *NH and NH_3 (mixed) and $*N_2H_4$ (alternating) (Figure 3a). The relative Gibbs energies of each reaction step on $Cu_{1.81}S(111)$ and Cu(111) are given in Table S4.

The potential-determining step (PDS) for the NRR on Cu(111) is the protonation of N_2 ($*N_2 \rightarrow *N_2H$; * denotes a surface site), and its limiting potential (U_L) is as high as 2.5 eV along with endothermic N_2 adsorption (Figure 3c), indicating that Cu(111) is unfavorable for the NRR, as observed in Figure 2g. If the same convention is considered over $Cu_{1.81}S$, U_L is large (2.0 eV), although the PDS is the same as that in the Cu case (I → II in Figure 3a), from which it is difficult to explain the high NRR activity for $Cu_{1.81}S$ shown in Figure 2g. Here, we propose a "bioinspired" pathway, where, instead of

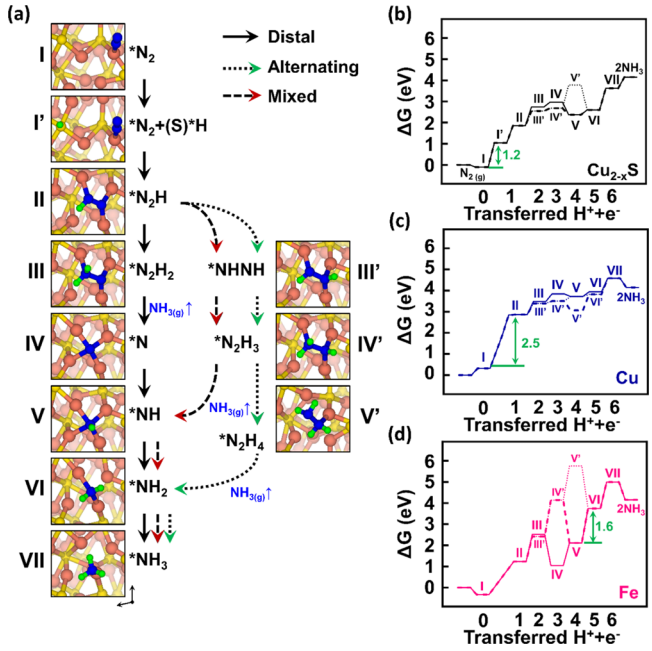

Figure 3. (a) NRR pathways depicted by the relaxed structure of intermediates on the tetragonal $Cu_{1.81}S$ surface. Here, the color code for atoms is Cu = coral, S = yellow, N = blue, and H = green. Free-energy diagrams of the NRR on (b) tetragonal $Cu_{2-x}S(111)$, (c) Cu(111), and (d) Fe(011) at pH = 13.3 and U = 0 V (vs RHE). The PDS for the NRR on each surface is depicted.

the direct protonation of $*N_2$, a sulfur site on $Cu_{1.81}S(111)$ is first protonated (I → I′ in Figure 3a), and then $*N_2$ is protonated via the transfer of H^+ bonded to sulfur (I′ → II). This pathway is very similar to the $N_2 \rightarrow N_2H$ protonation step of nitrogenase, where the H^+ source is a sulfur site on the Fe–Mo cofactor;[9] therefore, our mechanism can be called "bioinspired". Following the bioinspired pathway, sulfur protonation (I → I′ in Figure 3a) can be the PDS, with a greatly reduced U_L of 1.2 eV (Figure 3b). Here, the reaction barrier for the hydrogen transfer from Cu to S is 0.87 eV, which is still lower than U_L (1.2 eV). This reveals that the hydrogen transfer is readily feasible. In addition, we note that N_2H is horizontally adsorbed by three Cu atoms over $Cu_{1.81}S(111)$ in addition to the formation of a N–H···S hydrogen bond, which leads to further stabilization of the reactant of the PT reaction (I′ → II in Figure 3a) and then a more favorable NRR by reducing the free energy of this reaction (Figure S10). Similar behaviors are also observed for the $*N_2H_x$ (x = 2–4) adsorption species generated by further protonation. These observations clearly show that the threefold-coordinate Cu sites play a vital role in enhancing the NRR activity.

Moreover, although most NRR electrocatalysts follow one preferential pathway,[26] the threefold-coordinate Cu sites in $Cu_{1.81}S$ open two NRR pathways (Figure 4), which is another key factor to enhance the NRR activity. As presented in Figure 3b, the distal and mixed pathways show similar NRR energetics over $Cu_{1.81}S(111)$. The highest energy difference between the distal and mixed pathways is observed at the third protonation reaction for the distal ($*N_2H_2 \rightarrow *N$, III → VI in Figure 3a) and mixed/alternative ($*NHNH \rightarrow *NHNH_2$, III′ → VI′) pathways, which is very low (0.10 eV). This value is even lower than U_L (1.2 eV), indicating that the two pathways are readily possible. For comparison, the bcc Fe(011) surface was also

https://dx.doi.org/10.1021/acscatal.0c01730
ACS Catal. 2020, 10, 10577–10584

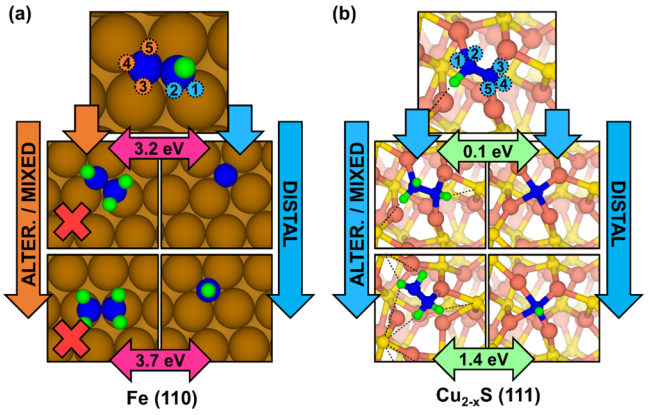

Figure 4. Schematic diagram for the hydrogen-bonding enhancement of the NRR activity in the $Cu_{2-x}S$ pathway. The NRR pathway for (a) Fe(110) and (b) tetragonal $Cu_{1.81}S(111)$ surfaces is depicted. Free-energy differences between the *N and *N_2H_3, and *NH and *N_2H_4, intermediates are compared. Only the distal mechanism can occur for Fe, whereas both distal and mixed mechanisms are possible for $Cu_{1.81}S(111)$ because of the stabilization of N_xH_y intermediates from the N−H···S hydrogen bonds (depicted as dotted lines). As a result, the number of effective active sites is increased for $Cu_{1.81}S$ compared to Fe.

considered. Over the surface, the highest energy difference between the NRR pathways is 3.2 eV at the third protonation, much higher than U_L (1.6 eV). This result reveals that the NH_3 generation over Fe(011) prefers only the distal process (Figure 4). Once *N_2 adsorbed on Fe(011) is protonated, the next possible protonation sites are only on the same nitrogen atom that is already protonated (depicted as the blue numbered circles in Figure 4a, the distal pathway), eventually limiting the active sites for a further protonation. However, on $Cu_{1.81}S$-(111), the reaction intermediates can be protonated for any nitrogen atom (depicted as the blue numbered circles in Figure 4b, the distal, mixed, and alternating pathways), increasing the number of effective active sites for protonation compared to Fe(011).

For efficient NRR electrocatalysts, the hydrogen evolution reaction (HER) must be suppressed. We calculated the HER potentials for every *H adsorption site over the tetragonal $Cu_{1.81}S(111)$ surface and found that the lowest HER barrier is 0.8 eV (Figure S11). In addition, the lowest *H passivation barrier over the $Cu_{1.81}S$ surface is 0.3 eV, which implies that the FE of NRR activity can be reduced by dominant hydrogen adsorption over the surface at the negative potentials than U = −0.3 V versus RHE. Note that the *N_2 adsorption free energy (−0.11 eV, Table S4) is lower than the lowest *H adsorption free energy (+0.3 eV, Figure S11) because of the basic condition (pH = 13.3), which explains why NRR occurs without hydrogen passivation of the active sites. In order to gain insight on the potential dependency of the NRR activity of the $Cu_{1.81}S$ catalyst, we compare the free-energy diagram when U is applied for the PDS or, more precisely, the rate-determining step (RDS) of the NRR and for HER on the S sites of the $Cu_{1.81}S(111)$ surface (Figure S12 and Table S5). It is well known that the free-energy barrier for the RDS (ΔG_{RDS}) goes down as U becomes negative for the NRR,[23] which is also observed in our calculations for U = 0.0 and −0.1 V versus RHE. However, the PT step is a nonelectrochemical reaction, which is not influenced by U. Consequently, ΔG for the PT step remains constant although U becomes negative, whereas ΔG_{RDS} for HER becomes lower. ΔG_{RDS} for HER becomes lower than that for the PT step at $U \leq -0.2$ V versus RHE (ΔG_{RDS} = 0.6 ± 0.1 eV for HER, 0.8 eV for PT), which indicates that HER should be dominant for $U \leq -0.2$ V and explains why the activity and FE for the NRR drop in the region of $U \leq -0.2$ V versus RHE (Figure S12c). HER can be suppressed, employing reported strategies to improve the FE, including the use of aprotic[28] or ionic liquid[29] electrolytes, and K^+ promotors,[30] indicating that there is still room to further improve the FE of $Cu_{1.81}S$. In addition, we note that advanced in situ experiments[31,32] can be useful to further clarify our NRR mechanism involving the formation of S−H bonds and N_xH_y intermediates during the NRR.

In Figure 2g, the chalcocite Cu_2S even shows an NH_3 production rate as high as 1.79 μmol h^{-1} cm^{-2}. Although this value is lower than that of tetragonal $Cu_{1.81}S$, it is still higher than those observed in other metal sulfide and pure metal catalysts. We analyzed the densities of threefold-coordinate Cu sites in each copper sulfide structure (Table S2). Indeed, $Cu_{1.81}S$ includes the most threefold Cu sites (0.10 $Å^{-3}$), followed by Cu_2S (0.03 $Å^{-3}$) and CuS (0.01 $Å^{-3}$), which matches well with the experimental NRR activity trend shown in Figure 2. This reveals why $Cu_{1.81}S$ has a higher activity than Cu_2S, although $Cu_{1.81}S$ has a lower Cu/S ratio. This result clearly supports the importance of the threefold-coordinate Cu sites for efficient NRR performance.

With the densities of the threefold-coordinate Cu sites, we can explain why CuS has generally a lower NRR activity compared to $Cu_{1.81}S$ and Cu_2S, but it still remains unclear why the NRR activity is actually higher than that of $Cu_{1.81}S$ and Cu_2S at U = 0.0 V versus RHE. Following the same procedure to $Cu_{1.81}S$, we determined the most stable surface for CuS(001) with DFT calculations and evaluated the free energies for HER and the first few steps of the NRR (Table S5). The initial protonation of the S site on CuS has a lower barrier (1.0 eV) compared to $Cu_{1.81}S$ (1.2 eV), which enables NRR at U = 0.0 V versus RHE. However, for a more negative U, the HER barrier on the S site of CuS (0.5 eV) is lower than that of $Cu_{1.81}S$ (0.8 eV); thus, the HER becomes more dominant on CuS than $Cu_{1.81}S$ as U becomes more negative.

We also note that copper sulfides can transform to copper oxides under aqueous ammonia and basic conditions.[33] However, this degradation of copper sulfides can be overcome via the introduction of an additive and a post-treatment of the electrode, which will be reported in the near future.

4. CONCLUSIONS

In summary, to further reproduce the NRR mechanism of nitrogenase over previous Fe- or Mo-based metal sulfides and then enhance the NRR performance, $Cu_{2-x}S$ ($0 \leq x < 1$) catalysts have been explored, in which a higher number of active metal sites is intended, considering that Cu can exhibit an oxidation number as low as 1, leading to a variety of $Cu_{2-x}S$ structures in contrast to those observed in the Fe- or Mo-based metal sulfides. Indeed, the $Cu_{1.81}S$ electrocatalyst shows a high production rate of 2.19 μmol h^{-1} cm^2 with a FE of 14.1% at −0.1 V versus RHE, which is higher than those of other metal sulfides. DFT calculations demonstrated the key role of the threefold-coordinate Cu sites in facilitating the activation of N_2 molecules, which enabled two reaction paths for the NRR, and the sites can also stabilize N_2H_y intermediates during the NRR process via N−H···S hydrogen-bonding interactions on the $Cu_{2-x}S$ surfaces. This study provides us with attractive low-cost

https://dx.doi.org/10.1021/acscatal.0c01730
ACS Catal. 2020, 10, 10577−10584

electrocatalysts for efficient NRR under ambient conditions and opens up an alternative route to explore transition-metal sulfides as NRR catalysts for NH_3 electrosynthesis.

■ ASSOCIATED CONTENT

Supporting Information

The Supporting Information is available free of charge at https://pubs.acs.org/doi/10.1021/acscatal.0c01730.

Details on experimental and computational methods, and additional results and discussions (PDF)

■ AUTHOR INFORMATION

Corresponding Authors

Sang Soo Han − *Computational Science Research Center, Korea Institute of Science and Technology, Seoul 02792, Republic of Korea;* orcid.org/0000-0002-7925-8105; Email: sangsoo@kist.re.kr

Seung Yong Lee − *Materials Architecturing Research Center, Korea Institute of Science and Technology, Seoul 02792, Republic of Korea;* orcid.org/0000-0002-6935-9439; Email: patra@kist.re.kr

Hyun S. Park − *Center for Hydrogen Fuel Cell Research, Korea Institute of Science and Technology, Seoul 02792, Republic of Korea;* orcid.org/0000-0002-7960-9729; Email: hspark@kist.re.kr

Authors

Min-Cheol Kim − *Computational Science Research Center, Korea Institute of Science and Technology, Seoul 02792, Republic of Korea;* orcid.org/0000-0002-4457-7421

Hyunji Nam − *Materials Architecturing Research Center, Korea Institute of Science and Technology, Seoul 02792, Republic of Korea; Department of Chemical and Biological Engineering, Korea University, Seoul 02841, Republic of Korea*

Jihyun Choi − *Center for Hydrogen Fuel Cell Research, Korea Institute of Science and Technology, Seoul 02792, Republic of Korea; Department of Chemical and Biomolecular Engineering, Yonsei University, Seoul 03722, Republic of Korea*

Hee Soo Kim − *Center for Hydrogen Fuel Cell Research, Korea Institute of Science and Technology, Seoul 02792, Republic of Korea*

Hong Woo Lee − *Computational Science Research Center, Korea Institute of Science and Technology, Seoul 02792, Republic of Korea; Department of Chemical and Biological Engineering, Korea University, Seoul 02841, Republic of Korea*

Donghun Kim − *Computational Science Research Center, Korea Institute of Science and Technology, Seoul 02792, Republic of Korea;* orcid.org/0000-0003-0326-5381

Jimin Kong − *Center for Hydrogen Fuel Cell Research, Korea Institute of Science and Technology, Seoul 02792, Republic of Korea; Department of Chemical and Biomolecular Engineering, Yonsei University, Seoul 03722, Republic of Korea;* orcid.org/0000-0003-2857-5984

Complete contact information is available at: https://pubs.acs.org/10.1021/acscatal.0c01730

Author Contributions

#M.-C.K., H.N., and J.C. contributed equally to this work.

Notes

The authors declare no competing financial interest.

■ ACKNOWLEDGMENTS

This work was supported by the Creative Materials Discovery Program through the National Research Foundation of Korea (NRF-2016M3D1A1021141).

■ REFERENCES

(1) Erisman, J. W.; Sutton, M. A.; Galloway, J.; Klimont, Z.; Winiwarter, W. How a Century of Ammonia Synthesis Changed the World. *Nat. Geosci.* **2008**, *1*, 636−639.

(2) Rod, T. H.; Logadottir, A.; Nørskov, J. K. Ammonia Synthesis at Low Temperatures. *J. Chem. Phys.* **2000**, *112*, 5343−5347.

(3) Chen, J. G.; Crooks, R. M.; Seefeldt, L. C.; Bren, K. L.; Bullock, R. M.; Darensbourg, M. Y.; Holland, P. L.; Hoffman, B.; Janik, M. J.; Jones, A. K.; Kanatzidis, M. G.; King, P.; Lancaster, K. M.; Lymar, S. V.; Pfromm, P.; Schneider, W. F.; Schrock, R. R. Beyond fossil fuel-driven nitrogen transformations. *Science* **2018**, *360*, eaar6611.

(4) Foster, S. L.; Bakovic, S. I. P.; Duda, R. D.; Maheshwari, S.; Milton, R. D.; Minteer, S. D.; Janik, M. J.; Renner, J. N.; Greenlee, L. F. Catalysts for Nitrogen Reduction to Ammonia. *Nat. Catal.* **2018**, *1*, 490−500.

(5) Wang, L.; Xia, M.; Wang, H.; Huang, K.; Qian, C.; Maravelias, C. T.; Ozin, G. A. Greening Ammonia toward the Solar Ammonia Refinery. *Joule* **2018**, *2*, 1055−1074.

(6) Suryanto, B. H. R.; Du, H.-L.; Wang, D.; Chen, J.; Simonov, A. N.; MacFarlane, D. R. Challenges and Prospects in the Catalysis of Electroreduction of Nitrogen to Ammonia. *Nat. Catal.* **2019**, *2*, 290−296.

(7) Zhou, J.-H.; Zhang, Y.-W. Metal-Based Heterogeneous Electrocatalysts for Reduction of Carbon Dioxide and Nitrogen: Mechanisms, Recent Advances and Perspective. *React. Chem. Eng.* **2018**, *3*, 591−625.

(8) Burgess, B. K.; Lowe, D. J. Mechanism of Molybdenum Nitrogenase. *Chem. Rev.* **1996**, *96*, 2983−3012.

(9) Raugei, S.; Seefeldt, L. C.; Hoffman, B. M. Critical Computational Analysis Illuminates the Reductive-Elimination Mechanism that Activates Nitrogenase for N_2 Reduction. *Proc. Natl. Acad. Sci. U.S.A.* **2018**, *115*, E10521−E10530.

(10) Feng, D.; Zhang, X.; Sun, Y.; Ma, T. Surface-Defective FeS_2 for Electrochemical NH_3 Production under Ambient Conditions. *Nano Mater. Sci.* **2020**, *2*, 132−139.

(11) Lashgari, M.; Zeinalkhani, P. Ammonia Photosynthesis under Ambient Conditions Using an Efficient Nanostructured FeS_2/CNT Solar-Energy-Material with Water Feedstock and Nitrogen Gas. *Nano Energy* **2018**, *48*, 361−368.

(12) Li, X.; Ren, X.; Liu, X.; Zhao, J.; Sun, X.; Zhang, Y.; Kuang, X.; Yan, T.; Wei, Q.; Wu, D. A MoS_2 Nanosheet−Reduced Graphene Oxide Hybrid: an Efficient Electrocatalyst for Electrocatalytic N_2 Reduction to NH_3 under Ambient Conditions. *J. Mater. Chem. A* **2019**, *7*, 2524−2528.

(13) Guo, Y.; Yao, Z.; Timmer, B. J. J.; Sheng, X.; Fan, L.; Li, Y.; Zhang, F.; Sun, L. Boosting Nitrogen Reduction Reaction by Bio-Inspired FeMoS Containing Hybrid Electrocatalyst over a Wide pH Range. *Nano Energy* **2019**, *62*, 282−288.

(14) Furuya, N.; Yoshiba, H. Electroreduction of Nitrogen to Ammonia on Gas-Diffusion Electrodes Loaded with Inorganic Catalyst. *J. Electroanal. Chem. Interfacial Electrochem.* **1990**, *291*, 269−272.

(15) Abghoui, Y.; Sigtryggsson, S. B.; Skúlason, E. Biomimetic Nitrogen Fixation Catalyzed by Transition Metal Sulfide Surfaces in an Electrolytic Cell. *ChemSusChem* **2019**, *12*, 4265−4273.

(16) Kresse, G.; Furthmüller, J. Efficiency of Ab-Initio Total Energy Calculations for Metals and Semiconductors Using a Plane-Wave Basis Set. *Comput. Mater. Sci.* **1996**, *6*, 15−50.

(17) Hammer, B.; Hansen, L. B.; Nørskov, J. K. Improved Adsorption Energetics Within Density-Functional Theory Using Revised Perdew-Burke-Ernzerhof Functionals. *Phys. Rev. B* **1999**, *59*, 7413−7421.

(18) Grimme, S.; Antony, J.; Ehrlich, S.; Krieg, H. A Consistent and Accurate Ab Initio Parametrization of Density Functional Dispersion Correction (DFT-D) for the 94 elements H-Pu. *J. Chem. Phys.* **2010**, *132*, 154104.
(19) Kresse, G.; Joubert, D. From Ultrasoft Pseudopotentials to the Projector Augmented-Wave Method. *Phys. Rev. B* **1999**, *59*, 1758−1775.
(20) Sheppard, D.; Terrell, R.; Henkelman, G. Optimization Methods for Finding Minimum Energy Paths. *J. Chem. Phys.* **2008**, *128*, 134106.
(21) Zimmer, D.; Ruiz-Fuertes, J.; Bayarjargal, L.; Haussühl, E.; Winkler, B.; Zhang, J.; Jin, C. Q.; Milman, V.; Alig, E.; Fink, L. Phase Transition of Tetragonal Copper Sulfide Cu_2S at Low Temperatures. *Phys. Rev. B* **2017**, *96*, 054108.
(22) Nørskov, J. K.; Rossmeisl, J.; Logadottir, A.; Lindqvist, L.; Kitchin, J. R.; Bligaard, T.; Jónsson, H. Origin of the Overpotential for Oxygen Reduction at a Fuel-Cell Cathode. *J. Phys. Chem. B* **2004**, *108*, 17886−17892.
(23) Skúlason, E.; Bligaard, T.; Gudmundsdóttir, S.; Studt, F.; Rossmeisl, J.; Abild-Pedersen, F.; Vegge, T.; Jónsson, H.; Nørskov, J. K. A Theoretical Evaluation of Possible Transition Metal Electro-Catalysts for N_2 Reduction. *Phys. Chem. Chem. Phys.* **2012**, *14*, 1235−1245.
(24) Zhang, L.; Ji, X.; Ren, X.; Ma, Y.; Shi, X.; Tian, Z.; Asiri, A. M.; Chen, L.; Tang, B.; Sun, X. Electrochemical Ammonia Synthesis via Nitrogen Reduction Reaction on a MoS_2 Catalyst: Theoretical and Experimental Studies. *Adv. Mater.* **2018**, *30*, 1800191.
(25) Montoya, J. H.; Tsai, C.; Vojvodic, A.; Nørskov, J. K. The Challenge of Electrochemical Ammonia Synthesis: A New Perspective on the Role of Nitrogen Scaling Relations. *ChemSusChem* **2015**, *8*, 2180−2186.
(26) Guo, X.; Gu, J.; Hu, X.; Zhang, S.; Chen, Z.; Huang, S. Coordination Tailoring towards Efficient Single-Atom Catalysts for N_2 Fixation: A Case Study of Iron-Nitrogen-Carbon (Fe@N-C) Systems. *Catal. Today* **2020**, *350*, 91−99.
(27) Xia, L.; Yang, J.; Wang, H.; Zhao, R.; Chen, H.; Fang, W.; Asiri, A. M.; Xie, F.; Cui, G.; Sun, X. Sulfur-Doped Graphene for Efficient Electrocatalytic N_2-to-NH_3 Fixation. *Chem. Commun.* **2019**, *55*, 3371−3374.
(28) Suryanto, B. H. R.; Kang, C. S. M.; Wang, D.; Xiao, C.; Zhou, F.; Azofra, L. M.; Cavallo, L.; Zhang, X.; MacFarlane, D. R. Rational Electrode−Electrolyte Design for Efficient Ammonia Electrosynthesis under Ambient Conditions. *ACS Energy Lett.* **2018**, *3*, 1219−1224.
(29) Zhou, F.; Azofra, L. M.; Ali, M.; Kar, M.; Simonov, A. N.; McDonnell-Worth, C.; Sun, C.; Zhang, X.; MacFarlane, D. R. Electro-Synthesis of Ammonia from Nitrogen at Ambient Temperature and Pressure in Ionic Liquids. *Energy Environ. Sci.* **2017**, *10*, 2516−2520.
(30) Hao, Y.-C.; Guo, Y.; Chen, L.-W.; Shu, M.; Wang, X.-Y.; Bu, T.-A.; Gao, W.-Y.; Zhang, N.; Su, X.; Feng, X.; Zhou, J.-W.; Wang, B.; Hu, C.-W.; Yin, A.-X.; Si, R.; Zhang, Y.-W.; Yan, C.-H. Promoting Nitrogen Electroreduction to Ammonia with Bismuth Nanocrystals and Potassium Cations in Water. *Nat. Catal.* **2019**, *2*, 448−456.
(31) Yao, Y.; Zhu, S.; Wang, H.; Li, H.; Shao, M. A Spectroscopic Study on the Nitrogen Electrochemical Reduction Reaction on Gold and Platinum Surfaces. *J. Am. Chem. Soc.* **2018**, *140*, 1496−1501.
(32) Yao, Y.; Zhu, S.; Wang, H.; Li, H.; Shao, M. A Spectroscopic Study of Electrochemical Nitrogen and Nitrate Reduction on Rhodium Surfaces. *Angew. Chem., Int. Ed.* **2020**, *59*, 10479−10483.
(33) Filmer, A.; Parker, A.; Clare, B.; Wadley, L. Oxidation of Copper Sulfides in Aqueous Ammonia. III. Kinetic Characteristics. *Aust. J. Chem.* **1979**, *32*, 2597−2609.

https://dx.doi.org/10.1021/acscatal.0c01730
ACS Catal. 2020, 10, 10577−10584